Nanoscale

PAPER

Cite this: *Nanoscale*, 2020, **12**, 8997

Valley-dependent topologically protected elastic waves using continuous graphene membranes on patterned substrates†

Jaehyung Hong,[a] Joo Hwan Oh,[a] Harold S. Park*[b] and Sung Youb Kim *[a]

Received 18th November 2019,
Accepted 2nd April 2020

DOI: 10.1039/c9nr09809g

rsc.li/nanoscale

We present a novel structure for topologically protected propagation of mechanical waves in a continuous, elastic membrane using an analog of the quantum valley Hall effect. Our system involves a thin, continuous graphene monolayer lying on a pre-patterned substrate, and as such, it can be employed across multiple length scales ranging from the nano to macroscales. This enables it to support topologically-protected waves at frequencies that can be tuned from the kHz to GHz range by either selective pre-tensioning of the overlaying membrane, or by increasing the lattice parameter of the underlying substrate. We show through numerical simulations that this continuous system is robust against imperfections, is immune to backscattering losses, and supports topologically-protected wave propagation along all available paths and angles. We demonstrate the ability to support topologically-protected interface modes using monolayer graphene, which does not intrinsically support topologically non-trivial elastic waves.

Introduction

Topological insulators have recently attracted significant attention due to their potential for the lossless propagation of various forms of wave energy.[1–3] These topological properties have been uncovered using both theoretical predictions and experimental observations of spin–orbit interactions that preserve time reversal symmetry (TRS) for electronic systems,[4–8] even for photonic and phononic systems.[9,10] Topological states enable a system to have back scattering-immunity, unidirectional energy transport, or even superconducting features. Although these exotic phenomena arise from fermions following Fermi–Dirac statistics, these concepts have recently been extended to photons,[11–15] and even to phonons[16–20] through analogy with the quantum hall family which are characterized from bosonic systems.

While most attention has focused on electronic topological insulators, topological phonons have attracted increasing visibility in recent years. As phonons represent the vibrational characteristic of solid lattice structures, they have drawn great interest because of their wide applicability across multiple length scales, and because of the relative ease in controlling the phononic band structure as compared to photonic or electronic systems. Because the low group velocity, high density of states, and relatively large impedance contrast implies that phononic systems are highly sensitive to disorder in wave propagation by scattering,[21,22] achieving topologically protected states in phononic systems is an important goal for solid structures. Although the differences from electrons such as the absence of spin–orbit interactions leads to challenges in achieving topological order in phononic systems, recent works have successfully found analogs of the quantum Hall family, for example the quantum spin hall effect (QSHE), to manipulate unit cells in order to generate double Dirac-cone dispersion using zone-folding techniques and degenerate pseudo-spin intact TRS.[23–27]

Recent studies on valley hall polarized mechanical states have enabled phononic structures to have distinct topological states preserving TRS without the pseudo-spin states that result in a phononic analog of the quantum valley Hall effect (QVHE).[28–31] The valley dependent topological states can be achieved through simple control of the unit cell geometry by breaking inversion symmetry. A large separation in momentum space and counter propagation at the corresponding symmetry point enables the structure to have backscattering immunity and unidirectional wave propagation. Because of the simple construction for topological phase classification, various space inversion symmetry (SIS) breaking systems in solids have been investigated such as bilayered lattices, vein-connected lattices, and diatomic lattices with resonant components.[32–35] However, we currently lack a design that can be scaled across length scales ranging from the nano to the macroscales, and thus the ability to function at frequencies ranging from the kHz to GHz ranges.[36–39] Furthermore, we

[a]*Department of Mechanical Engineering, Ulsan National Institute of Science and Technology, Ulsan 44919, Republic of Korea. E-mail: sykim@unist.ac.kr*
[b]*Department of Mechanical Engineering, Boston University, Boston, MA 02215, USA. E-mail: parkhs@bu.edu*

†Electronic supplementary information (ESI) available. See DOI: 10.1039/c9nr09809g

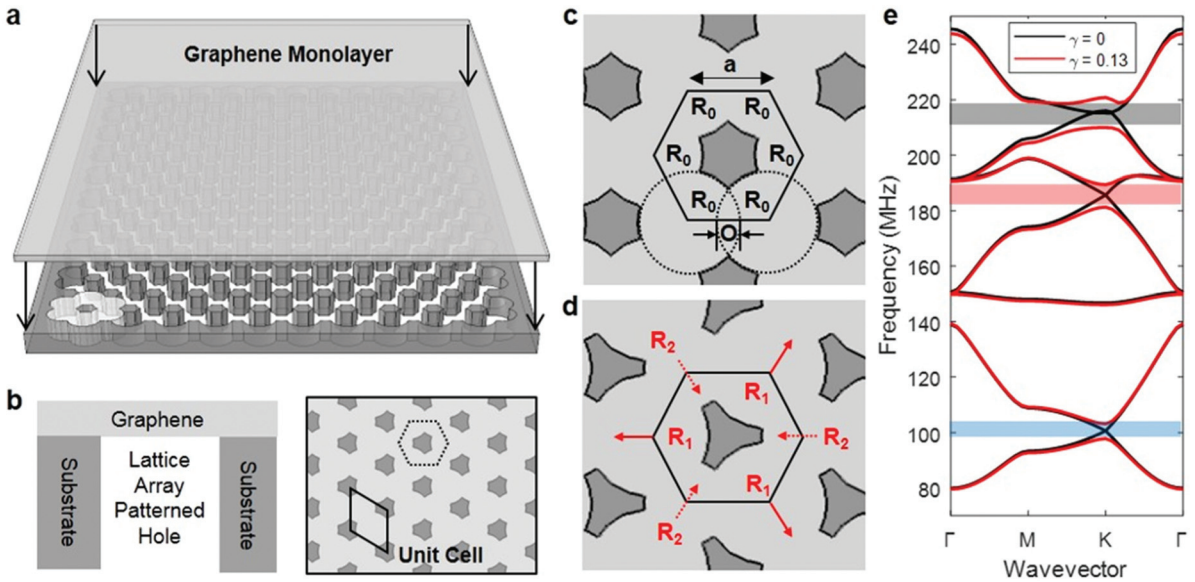

Fig. 1 Achieving topologically-protected elastic wave propagation using continuous graphene membranes on patterned substrates. (a) Design concept of patterned membrane. The substrate is pre-patterned with a lattice of arrayed holes (white), after which the graphene membrane is laid on top of it. (b) Side view (left) of the structure that supports a free-standing graphene membrane on a lattice arrayed hole and top view (right) of continuous two dimensional phononic crystal lattice structure, with the hexagonal lattice array shown in dashed black lines and the unit cell for dispersion calculations shown in solid black lines. (c) Hexagonal symmetry lattice structure with constant lattice parameter. (d) Breaking space inversion symmetry by increasing $R_1 = R_0 + d$ and decreasing $R_2 = R_0 - d$. (e) Frequency dispersion curve for symmetric case, R_0 = 3 μm (black solid lines) and asymmetric cases R_1 = 3.2 μm and R_2 = 2.8 μm (red solid lines) showing the emergence of bandgap opening for three different frequency regimes.

lack the ability to actively tune the topologically-protected bandgap widths and frequencies once a structure has been fabricated. Finally, most proposed structures to-date are discontinuous in the plane, and require external, active elements to help achieve topologically non-trivial properties, which significantly complicates the fabrication and scalability of such concepts.[40–42]

Here, we present a novel concept for achieving topologically-protected elastic wave propagation based on the QVHE. We achieve this by considering, as shown in Fig. 1a, a pre-patterned periodic substrate with overlapping holes of radius R_0, thus creating an effective hexagonal lattice structure, on top of which is placed a solid, in-plane continuous two-dimensional membrane, such as monolayer graphene. It is well-known that pristine graphene does not possess a phononic bandgap, and that the intrinsic graphene lattice structure satisfying C_6 crystalline symmetry induces a Dirac-cone in the dispersion relationship at the K point of the Brillouin zone. In order to create a bandgap at the relevant frequency, we break SIS by varying the radius of the disk at each lattice site that results in reducing the order of crystalline symmetry from C_6 to C_3.

Results and discussion

Structural design concept

Topologically-speaking, this patterned substrate in the form of a diatomic graphene lattice results in a time-reversal-invariant system with large separation in momentum space between the K and K′ valleys where there exist two distinct frequency extrema in the band structure that embody valley-dependent non-trivial properties, thus resulting in a QVHE analog in a solid structure. Since our structure is constrained in the longitudinal directions, for example *via* van der Waals forces between graphene and an SiO_2 substrate,[43] it supports out-of-plane flexural waves and thus transverse phonon modes. The novelty of this design for nanomechanical devices is the geometrical simplicity and dimensional consistency, and the fact that it can immediately be fabricated experimentally, where only the substrate need be fabricated, and not the overlaying membrane. This allows for scalable customization for desired frequency ranges without any additional components such as resonant elements. Furthermore, this design is scale-invariant in the sense that it can be utilized at the nano or macroscales; for specificity we consider the membrane to be monolayer graphene in this work.

Phononic dispersion analysis

To examine the topological properties of this structure, we conducted finite element simulations using COMSOL Multiphysics to find the frequency dispersion of the Brillouin zone for a unit cell with a constant lattice parameter, a = 4.5 μm and symmetric radius, R_0 = 3 μm (Fig. 1d). The free-standing membrane has the elastic properties of monolayer graphene throughout this work and in our numerical simulations (see Methods).[44] We define a parameter γ that characterizes the order of SIS breaking which is defined as $\gamma = (R_1 -$

$R_2)/R_0$ where R_0 is the radius which makes the structure preserve SIS and R_1, R_2 are the radii at each diatomic lattice site. R_1 and R_2 are changed in complementary fashion, *i.e.* that R_1 increases when R_2 decreases in order to retain a constant lattice parameter (Fig. 1c and d). For a unit cell with $\gamma = 0$, which is the symmetric case, Dirac-cones in the band structure are observed around 100.6 MHz and 185.7 MHz at the K point in momentum space By varying the radius ratio γ from 0 to 0.13, a bandgap emerges at the K point, with a width of about 5.4 MHz (blue box) from 97.8 MHz to 103.2 MHz and 8.2 MHz (red box) from 181.3 MHz to 189.5 MHz (Fig. 1e). Also, while there exists another bandgap region around 210 MHz (black box), we focus on the lower frequencies in this work.

Visualization of the eigenvector mode shapes in momentum space for two identical structures which have chiral symmetry, $\gamma = 0.13$ and $\gamma = -0.13$ at each corresponding bandgap frequency range, reveals the topological phase transition with a degeneracy at the K point as shown in Fig. 2a. For $\gamma = 0$, the first Dirac point (100.6 MHz) represents the interaction of the monopole modes of each membrane and the second Dirac point (185.7 MHz) represents the interaction of the dipole modes of each membrane. With increasing γ from 0 to 0.13, polarization of the modes results in the interaction of monopole modes in the first bandgap region and monopole–dipole interactions in the second bandgap region (Fig. 2a). We implemented 2×2 supercells based on the unit cell containing at least one intact hexagonal lattice structure to determine these polarized modes in wave propagation throughout the structure (Fig. S1†). For $\gamma = -0.13$, wave propagation through the intact lattice structure at the K point of the Brillouin zone shows clockwise propagation in the lower band at a frequency of 97.8 MHz and counterclockwise propagation in upper band with 103.2 MHz frequency while it shows reversed propagation direction for $\gamma = 0.13$, *i.e.* being counterclockwise in the lower band and clockwise in the upper band with the same frequencies (ESI Video 1†), indicating the emergence of band inversion, which is essential for a topological phase transition. This inversion also emerges in the second bandgap region from 181.3 MHz to 189.5 MHz, again demonstrating that breaking SIS of the structure not only results in a bandgap, but also the emergence of band inversion which is essential for topological phase transition (ESI Video 2†).

Topological analysis

These topological phenomena are characterized by a topological invariant known as the Chern number, which is calculated by numerically integrating the Berry curvature over a small region near the K and K′ points (see Methods). The Berry curvatures calculated in the 1st Brillouin zone at $k_x = -2\pi/3$ are highly localized at the K and K′ points with opposite sign. These valley-dependent topological invariants are also reversed for the lower and upper bands in both bandgap regions (Fig. 2b and c). Since the valley Chern number, defined as $C_v = C_k - C_{k'}$, is non-zero and has opposite value, this valley-dependent Berry curvature shows that breaking SIS ensures a QVHE-like topological phase transition.

We also demonstrate in Fig. 2d and e the tunability of the frequency from the kHz to the GHz range by changing the lattice parameter a/a_0 of pre-patterned lattice substrate where a_0 is defined as $R_1 + R_2 - O$, where O is the overlapped length between two disks as shown in Fig. 1c, or from the MHz to GHz range by changing the pre-tension T/T_0 within the graphene membrane (see Methods for full definition of the lattice parameter). The values of the first and second bandgap regions are inversely proportional to the ratio of the lattice parameter, a/a_0, and directly proportional to the square root of pre-tension variation ratio, $(T/T_0)^{1/2}$ (Fig. 2d and e). It is worthwhile to note that the natural frequency of a circular membrane under the out-of-plane oscillation exhibits the same relationship and one can derive the relationship based on continuum membrane theory.[45] Because the overall frequency range increases with decreasing lattice parameter and increasing pre-tension, the bandgap width also increases at higher frequencies (smaller a/a_0). We checked the values of the topological invariants, which showed K-valley localization while being proportional to the square of the lattice parameter ratio while remaining constant for varying pre-tension (Fig. S2†), which demonstrates that the topological phase transition is still valid across multiple length scales and arbitrary pre-tension values. Therefore, we can use the lattice parameter of the patterned substrate and the pre-stress acting on the continuous graphene membrane to both achieve specific topologically-protected frequencies, while the pre-stress can be used to actively tune the topological frequencies and bandgaps of the overlaying membranes.

To verify the presence of topologically protected edge states, we conducted frequency domain simulations for three types of edges that are possible for the hexagonal lattice structure (Fig. S3a–S3c†): the two zigzag types (ZIG1 and ZIG2) and armchair type (ARM). For clarity, the structures corresponding to $\gamma = -0.13$ and $\gamma = 0.13$ are labeled as A type and B type such that ZIG1 and ZIG2 edge states are defined as interface of A–B type and B–A type respectively. Specifically, a ZIG1 edge contains two lattice structures with R_1 and a ZIG2 edge contains two lattice structure with R_2. We created a supercell composed of an A–B–A type, two hexagonal A types – four hexagonal B types – two hexagonal A types, for the frequency dispersion calculation with Bloch periodic condition in k_x direction (Fig. 3a). Edge states marked as red solid lines are states that cross the bandgap and intersect near the valley point K(K′) where $k = 2/3$ (4/3) (Fig. 3b). This clearly indicates the presence of a topologically non-trivial interface connecting the A–B and B–A states that support interface modes with distinct frequencies of 102 MHz and 186 MHz. The deformed mode shapes at valley frequencies show that these edge states are strongly localized within a single hexagonal lattice constant away from the interface at both 102 MHz and 186 MHz respectively, which facilitates topologically protected wave propagation through the interface (Fig. 3c and d).

In the case of ARM edges states, we add lattice components with radius R_0 in order to enhance symmetry (Fig. S4†). A supercell composed by the A–B interface is adopted for the fre-

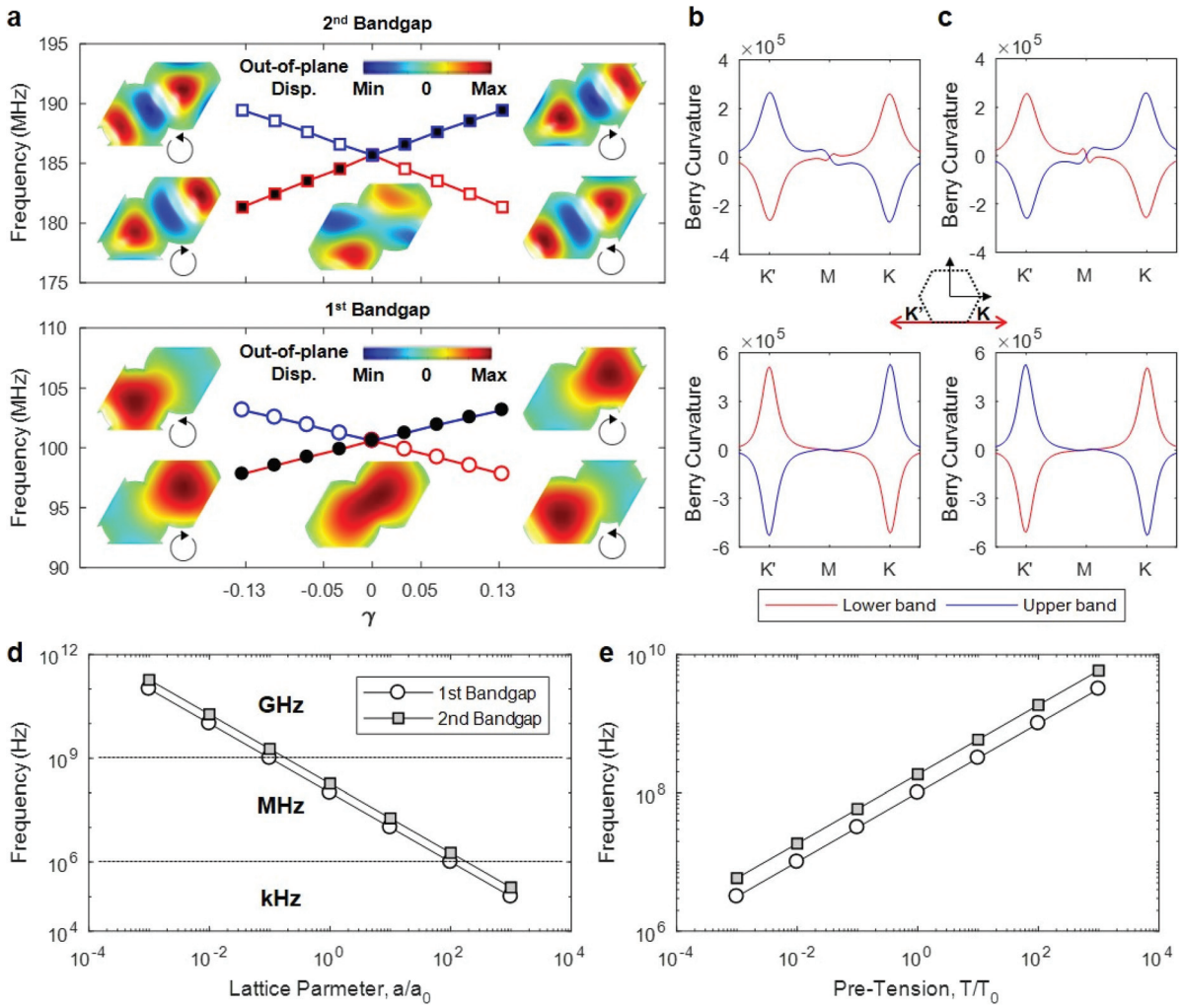

Fig. 2 Topological phase transition and frequency tunability. (a) Evolution of bandgap width with respect to increasing γ, where band inversion occurs at $\gamma = 0$. (Top) unit cell mode shapes at 185.7 MHz for different values of γ, (bottom) unit cell mode shapes at 100.6 MHz for different values of γ. Berry curvatures in the 1st Brillouin zone when $k_y = -2/3$ for (b) $\gamma = -0.13$ and (c) $\gamma = 0.13$ that indicates a valley-dependent Chern number which is reversed with inversion symmetry in the first bandgap region (bottom) and second bandgap region (top). Tunability of the bandgap frequencies by changing the (d) lattice parameter and (e) value of pre-tension where $a_0 = 4.5$ μm and $T_0 = 0.65$ N m^{-1}.

quency domain calculation in the same way as the ZIG edges (Fig. 3e). The frequency domain results show that the ARM edge also has gapless and strongly localized edge states (Fig. 3f and g). Since the rotation of Brillouin zone occurs in case of ARM edge lattice structure, the Dirac points and intersecting point of edge states in momentum space are shifted to the Γ point from the K point.

The wave propagation through topologically protected edge states in this system is clearly established through visualization of edge states propagation modes. For these edge states, forward propagating modes induced by ZIG1 (ZIG2) emerged from near K (K′) valley whereas backward propagating modes induced by ZIG1 (ZIG2) emerged from near K′ (K) valley (Fig. 3c and d). In more detail, for ZIG1 (ZIG2), the A-state shows clockwise propagating mode while B-state shows counterclockwise propagating mode (ESI Videos 3 and 4†). These counter propagating characteristics with a large interval in momentum space from K to K′ ensures valley-dependent interfacial wave propagation that represents an analogue to the QVHE, implying backscattering immunity as well as unidirectional wave propagating system. This demonstrates a topologically-protected waveguide where waves can travel unimpeded along all possible paths in a hexagonal lattice.

Full-field simulations

One of the significant features of a topologically protected waveguide system is robustness against imperfections such as sharp edge corners and defects. First, we implement a steady state frequency domain analysis in order to confirm immunity to backscattering at sharp edge corners. Four types of sharp edge corners are employed to demonstrate the ability to support all possible wave propagation paths in a hexagonal lattice. A triangle shaped closed waveguide composed of two identical single ZIG (ZIG1 and ZIG2) edges with 60° angles

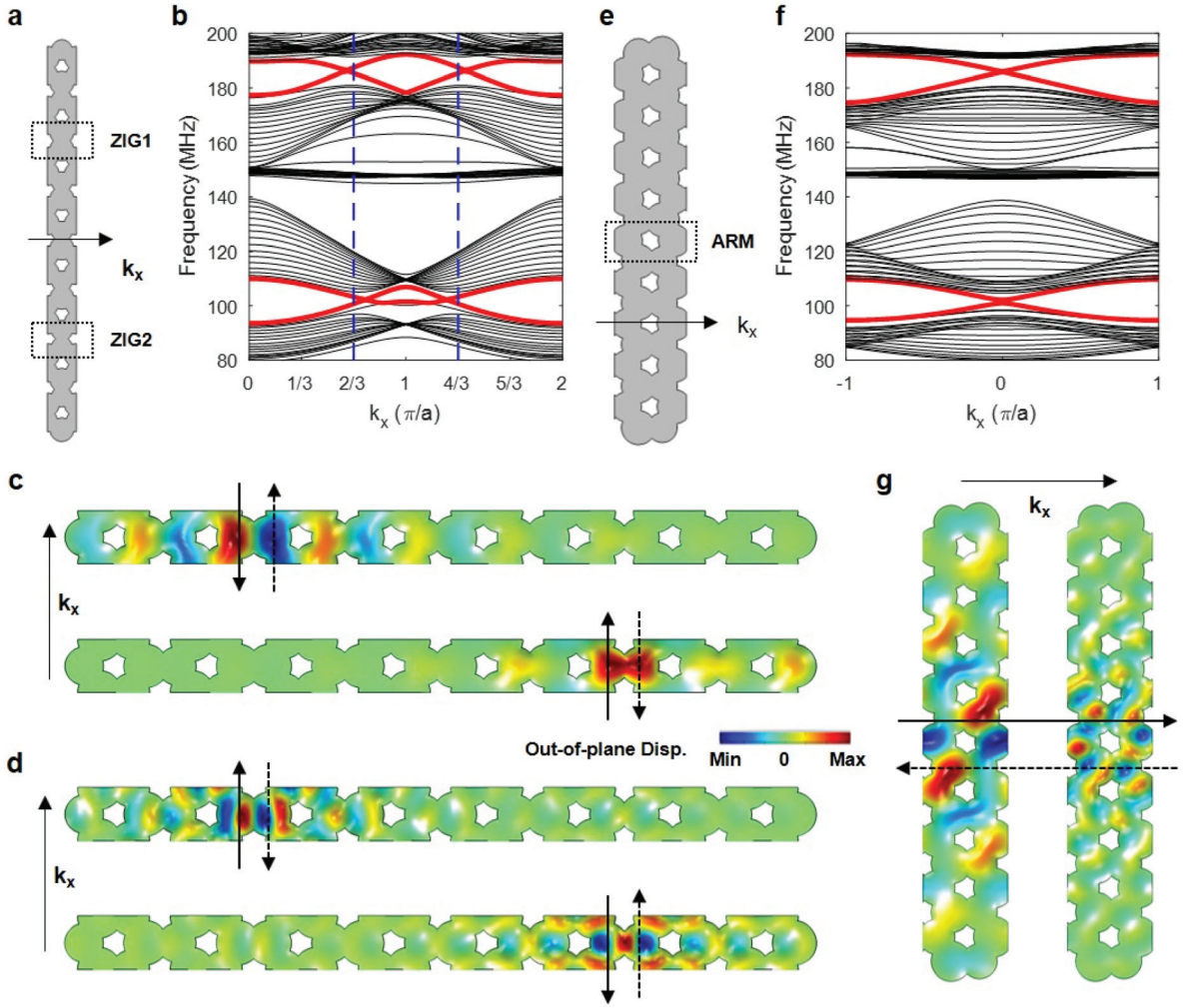

Fig. 3 Edge state frequency dispersion curve and mode shapes. (a) Supercell geometry for two ZIG type edges. (b) Frequency dispersion curve that shows counter-propagating edge states marked as red lines within the bandgap region. These edge states are localized near the interface lattice at (c) 102 MHz and (d) 187 MHz while also showing valley-dependent counter propagating modes at the K point (black solid arrow) and K′ point (black dashed arrow). (e) Supercell geometry for revised ARM type edge and (f) frequency dispersion curve that indicates similar (g) edge states to ZIG at 102 MHz (left) and 187 MHz (right). The counter propagating topological phase transition occurs near the Γ point, k_x = 0, for positive k_x (black solid arrow) and negative k_x (black dashed arrow).

(Fig. 4a), a parallelogram shaped closed waveguide composed of ZIG1 and ZIG2 edge with 120° angles (Fig. 4c) and a square shaped closed waveguide composed of ZIG and ARM with 90° angles (Fig. 4e) in 23 × 10 unit cells are adopted for verification of topologically protected wave propagation. The displacement field calculated from the frequency response for the excitation point (red circle) with topologically-protected frequencies 102 MHz and 186 MHz shows stable and strongly localized wave propagation through the topologically-protected interface for all sharp angle corners (Fig. 4b, d and f). This robustness to sharp bends enables arbitrarily complicated waveguides in practice. Moreover, in order to verify robustness to defects we deleted a single nanodrum near the path of ZIG in the triangular shaped closed waveguide (Fig. 4g). Likewise, at both topologically-protected frequencies 102 MHz and 186 MHz, the waveguide maintains their localized propagation (Fig. 4h), thus demonstrating robustness against imperfections by topologically protected states.

Another remarkable topological feature is unidirectional wave propagation by valley dependent counter-propagation. In order to clarify this, we composed four distinct domains consisting of two A states and two B states distinguished by ZIG1, ZIG2 and two ARM edge states (Fig. 5a), which induces wave propagation in the directions marked in yellow along the interfaces. Waves excited from the red (orange) point propagate in a topologically-protected manner first along the ZIG1 (ZIG2) edge, and subsequent along the ARM edge (Fig. 5b). Although the opposite edge state ZIG2 (ZIG1) has identical frequency dispersion, wave propagation through the opposite edge ZIG2 (ZIG1) is locked since the ZIG1 edge state supports upward wave propagation while ZIG2 supports downward wave propagation. Moreover, the phased excitation based on the phase of

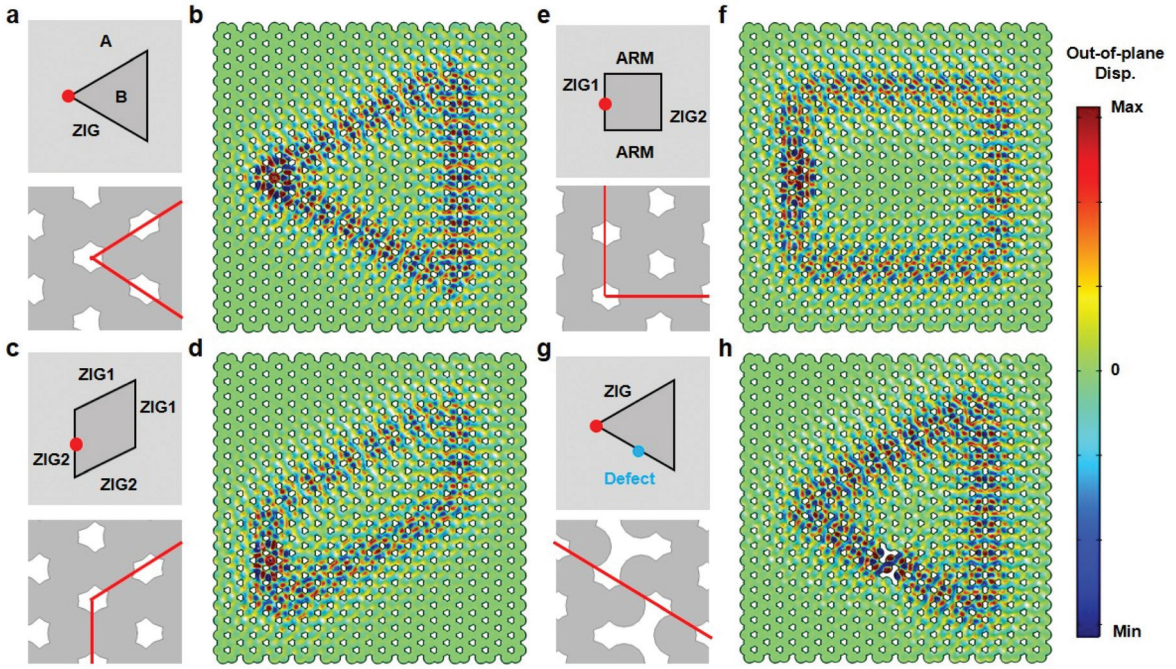

Fig. 4 Robustness to imperfections. Frequency domain analysis for various interface paths including sharp 60° degree turn for (a, b) single ZIG edge, with 60° and 120° degree turns for (c, d) two ZIG edges and with 90° degree turns for (e, f) two ZIG edges and two ARM edges. (g, h) Frequency domain analysis for when defects (blue) are introduced along the interface. (a, c, e, g) Interface edges excited are at 187 MHz and denoted as red lines in the bottom detailed lattice cut.

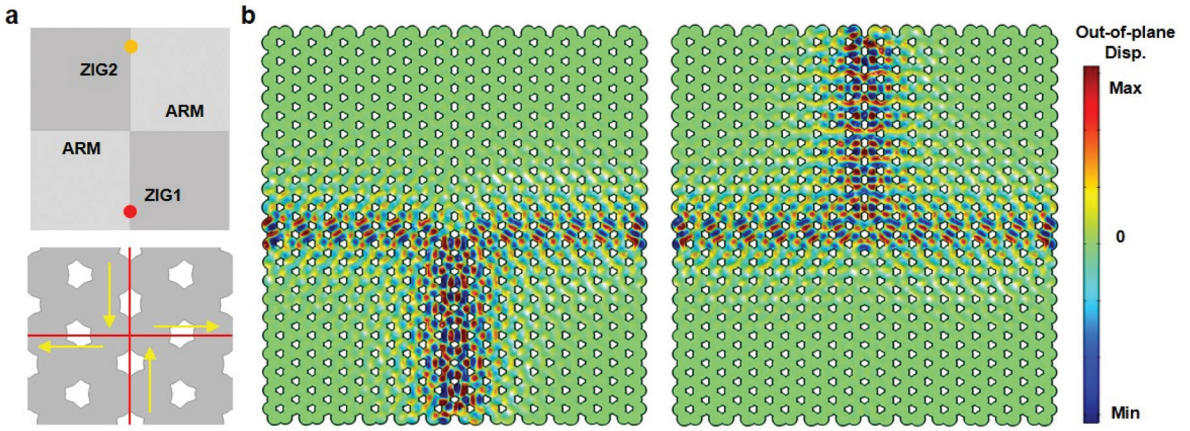

Fig. 5 Unidirectional wave propagation. (a) Frequency domain analysis at 187 MHz with four discretized domains with two identical states that yields different wave propagation directions as indicated by the yellow arrows. (b) Excited from ZIG1 (left) and excited from ZIG2 (right) show unidirectional wave propagation based on valley-dependent topological protection.

the out-of-plane displacement from edge dispersion results enables the one-way wave excitation along a single edge that enables separation of forward and backward propagating waves along the same edge (Fig. S5†). This propagating characteristic is analogous to pseudospin-dependent topological phase that ensures unidirectional wave propagation.

Finally, we verify the topologically-protected wave propagation using real-time finite element simulations *via* the commercial finite element code ABAQUS (see Methods). To demonstrate propagation over all available paths within the hexagonal lattice structure, we created an L-shaped path consisting of ZIG1, ZIG2, and ARM type edges as shown in Fig. 6a. A 40-count wave pulse with frequency of 186 MHz was used as the excitation on the ZIG2 edge. The wave pulse, which starts from the ZIG2 edge propagates through a 60° angle change to the next ZIG2 edge, after which a 120° angle change is made to propagate along the ZIG1 edge. Finally, a 90° angle change is made to propagate along the ARM edge. The snapshots of the

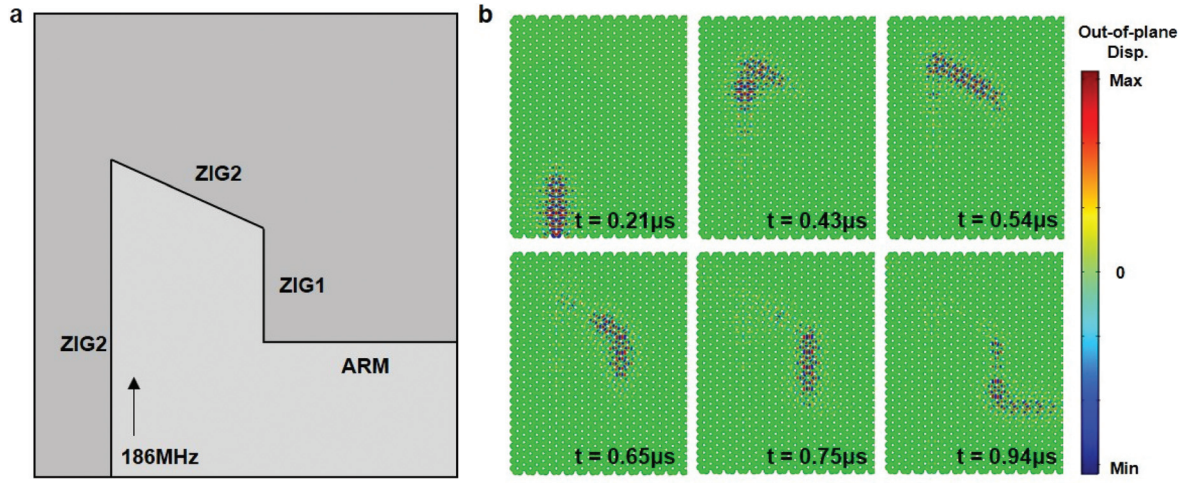

Fig. 6 Real-time wave propagation. (a) Waveguide comprised of all available edge types ZIG1, ZIG2, and ARM in the hexagonal lattice. (b) Wave propagation results at different times for 186 MHz excitation.

wave propagation at different times in Fig. 6b clearly indicate the absence of backscattering at sharp corners, with the energy transported along the interface. This result is completely consistent with the previously discussed valley-dependent characteristics and frequency domain results, demonstrating robustness to sharp turns and corners and unidirectional wave propagation.

Conclusions

In conclusion, we have presented and numerically validated a new design of a fully continuous phononic analog of the quantum valley hall effect. We accomplished this through a system consisting of a continuous solid membrane lying on a patterned substrate, which should enable this approach to be used across multiple length scales ranging from the nanoscale to the macroscale we demonstrated scalability of the achievable frequencies from the kHz to the GHz range by changing the lattice parameter of the patterned substrate, while also demonstrating significant tunability of the frequency for a set geometry by applying stress to the membrane. The numerical examples also demonstrated the ability to transport topologically-protected wave energy along arbitrary pathways in monolayer graphene, which does not intrinsically support topologically non-trivial elastic waves. Overall, the approach presented here represents a robust approach to enabling phononic topological devices across a range of technologically relevant length scales and operating frequencies.

Simulation methods

We performed finite element simulations to calculate the frequency dispersion relationship of our phononic crystal structure using COMSOL Multiphysics. We implemented a prestressed eigenfrequency analysis module based on membrane mechanics. The lattice parameter, a, can be changed with fixed ratio between R_1, R_2, and O, that is $2a = 2R_1 + 2R_2 - 2O$ for frequency tuning (see Fig. 1c and d). The material properties for monolayer graphene, which serves as the free-standing membrane in this work, are Young's modulus 1TPa, Poisson's ratio 0.165, density 2.267 g cm^{-3}, thickness 0.335 nm and isotropic in-plane pre-stress 0.65 N m^{-1}.[44] Since the continuous solid membrane is lying on the pre-patterned substrate, we design the unit cell similar to the substrate pattern and apply fixed boundary conditions on the patterned edges. We used a 2 × 2 unit cell for supercell in order to visualize the wave propagation.

We employ Floquet periodic boundary conditions to four periodic sides, $u(\boldsymbol{r} + \boldsymbol{R}) = u(\boldsymbol{r})\cdot\exp(i\boldsymbol{k}\cdot\boldsymbol{R})$ where $u(\boldsymbol{r})$ is the displacement vector, $\boldsymbol{r}$ is the position within a unit cell, $\boldsymbol{R}$ is a lattice translation vector and $\boldsymbol{k}$ is the wavevector. We calculate the frequency dispersion curves along the boundary of the irreducible 1st Brillouin zone in two dimensions. Likewise, we performed frequency domain simulations to verify the emergence of edge states along interfaces. The supercell has $n \times 1$ unit cell geometry and the frequency dispersion was calculated with periodic boundary conditions along the x-direction only. We also calculated the berry curvature in order to evaluate the topological invariant from the unit cell geometry as $\boldsymbol{\Omega}_n(\boldsymbol{k}) = \nabla\boldsymbol{k} \times \langle \boldsymbol{u}_n(\boldsymbol{k}) | i\nabla_{\mathbf{k}} | \boldsymbol{u}_n(\boldsymbol{k})\rangle$, where $\boldsymbol{u}$ is displacement vector field, k is the wavevector and n represents the nth mode. The local Chern number, $C_{K/K'}$, is calculated as $2\pi C = \int \Omega_n(k) d^2k$. Thus, a highly localized berry curvature at the K point gives signed local Chern number, ideally ±1/2. That is, the valley Chern number, $C_v = C_K - C_{K'}$, becomes ±1.

In addition, implicit dynamic finite element simulations are conducted to visualize real-time wave propagation through topologically protected waveguide using the commercial simulation code ABAQUS. 27 × 29 unit cells were used to create the L-shaped waveguide including ZIG1, ZIG2 and ARM edges, which represents all possible path in a hexagonal lattice. The entire domain is initialized with in-plane pre-stress and all external boundary edges are fixed. The wave pulse is initiated

by unit displacement, 0.001 nm, with target frequency, 186 MHz. We detected the wave propagation response for each time increment.

Conflicts of interest

There are no conflicts to declare.

Acknowledgements

We gratefully acknowledge the support from the Mid-Career Researcher Support Program (Grant No. 2019R1A2C2011312) of the National Research Foundation (NRF) of Korea and from the Meta-Structure Based Seismic Shielding Research Fund (Project No. 1.190100.01) of the UNIST. HSP acknowledges support from the ARO, grant W911NF-18-1-0380. We also acknowledge with gratitude the supercomputing resources of the UNIST Supercomputing Center.

References

1 M. Z. Hasan and C. L. Kane, *Rev. Mod. Phys.*, 2010, **82**, 3045–3067.
2 C. L. Kane and E. J. Mele, *Phys. Rev. Lett.*, 2005, **95**, 146802.
3 C. L. Kane and E. J. Mele, *Phys. Rev. Lett.*, 2005, **95**, 226801.
4 B. A. Bernevig, T. L. Hughes and S.-C. Zhang, *Science*, 2006, **314**, 1757–1761.
5 M. König, S. Wiedmann, C. Brüne, A. Roth, H. Buhmann, L. W. Molenkamp, X.-L. Qi and S.-C. Zhang, *Science*, 2007, **318**, 766.
6 L. Fu, C. L. Kane and E. J. Mele, *Phys. Rev. Lett.*, 2007, **98**, 106803.
7 J. E. Moore and L. Balents, *Phys. Rev. B: Condens. Matter Mater. Phys.*, 2007, **75**, 121306.
8 D. Hsieh, D. Qian, Y. Xia, Y. S. Hor, R. J. Cava and M. Z. Hasan, *Nature*, 2008, **452**, 970.
9 W. Jiang, M. Kang, H. Huang, H. Xu, T. Low and F. Liu, *Phys. Rev. B*, 2019, **12**, 125131.
10 H. Huang, W. Jiang, K.-H. Jin and F. Liu, *Phys. Rev. B*, 2018, **98**, 045131.
11 L. Lu, J. D. Joannopoulos and M. Soljačić, *Nat. Photonics*, 2014, **8**, 821–829.
12 A. B. Khanikaev, S. H. Mousavi, W.-K. Tse, M. Kargarian, A. H. MacDonald and G. Shvets, *Nat. Mater.*, 2013, **12**, 233–239.
13 M. Hafezi, S. Mittal, J. Fan, A. Migdall and J. M. Taylor, *Nat. Photonics*, 2013, **7**, 1001–1005.
14 M. C. Rechtsman, J. M. Zeuner, Y. Plotnik, Y. Lumer, D. Podolsky, F. Dreisow, S. Nolte, M. Segev and A. Szameit, *Nature*, 2013, **496**, 196–200.
15 A. B. Khanikaev and G. Shvets, *Nat. Photonics*, 2017, **11**, 763.
16 P. Wang, L. Lu and K. Bertoldi, *Phys. Rev. Lett.*, 2015, **115**, 104302.
17 S. H. Mousavi, A. B. Khanikaev and Z. Wang, *Nat. Commun.*, 2015, **6**, 9682.
18 J. Cha, K. W. Kim and C. Daraio, *Nature*, 2018, **564**, 229–233.
19 S.-Y. Yu, C. He, Z. Wang, F.-K. Liu, X.-C. Sun, Z. Li, H.-Z. Lu, M.-H. Lu, X.-P. Liu and Y.-F. Chen, *Nat. Commun.*, 2018, **9**, 3072.
20 S. D. Huber, *Nat. Phys.*, 2016, **12**, 621–623.
21 S. G. Johnson, M. L. Povinelli, M. Soljačić, A. Karalis, S. Jacobs and J. D. Joannopoulos, *Appl. Phys. B*, 2005, **81**, 283–293.
22 J. P. Wolfe, *Imaging Phonons: Acoustic Wave Propagation in Solids*, Cambridge Univ. Press, Cambridge, 2005.
23 R. Süsstrunk and S. D. Huber, *Science*, 2015, **349**, 47–50.
24 G. Salerno, A. Berardo, T. Ozawa, H. M. Price, L. Taxis, N. M. Pugno and L. Carusotto, *New J. Phys.*, 2017, **19**, 055001.
25 R. Chaunsali, C. W. Chen and J. Yang, *Phys. Rev. B*, 2018, **97**, 054307.
26 L.-Y. Zheng, G. Theocharis, V. Tournat and V. Gusev, *Phys. Rev. B*, 2018, **97**, 060101.
27 M. Miniaci, R. K. Pal, B. Morvan and M. Ruzzene, *Phys. Rev. X*, 2018, **8**, 031074.
28 J. Lu, C. Qiu, L. Ye, X. Fan, M. Ke, F. Zhang and Z. Liu, *Nat. Phys.*, 2017, **13**, 369–374.
29 R. K. Pal and M. Ruzzene, *New J. Phys.*, 2017, **19**, 025001.
30 J. Vila, R. K. Pal and M. Ruzzene, *Phys. Rev. B*, 2017, **96**, 134307.
31 J. W. Jiang, B. S. Wang and H. S. Park, *Nanoscale*, 2018, **10**, 13913.
32 S. Y. Huo, J. J. Chen, H. B. Huang and G. L. Huang, *Sci. Rep.*, 2017, **7**, 10335.
33 R. K. Pal, M. Schaeffer and M. Ruzzene, *J. Appl. Phys.*, 2016, **119**, 084305.
34 J. Wang and J. Mei, *Appl. Phys. Express*, 2018, **11**, 057302.
35 H. Zhu, T. W. Liu and F. Semperlotti, *Phys. Rev. B*, 2018, **97**, 174301.
36 B. H. Nguyen, X. Zhuang, H. S. Park and T. Rabczuk, *J. Appl. Phys.*, 2019, **125**, 095106.
37 T. Liu and F. Semperlotti, *Phys. Rev. Appl.*, 2018, **9**, 014001.
38 R. Süsstrunk, P. Zimmermann and S. D. Huber, *New J. Phys.*, 2017, **19**, 015013.
39 S. Li, D. Zhao, H. Niu, X. Zhu and J. Zang, *Nat. Commun.*, 2018, **9**, 1370.
40 M. Yan, J. Lu, F. Li, W. Deng, X. Huang, J. Ma and Z. Liu, *Nat. Mater.*, 2018, **17**, 993–998.
41 Y. Wu, R. Chaunsali, H. Yasuda, K. Yu and J. Yang, *Sci. Rep.*, 2018, **8**, 112.
42 B.-Z. Xia, S.-J. Zheng, T.-T. Liu, J.-R. Jiao, N. Chen, H.-Q. Dai, D.-J. Yu and J. Liu, *Phys. Rev. B*, 2018, **97**, 155124.
43 J. Bunch, S. Verbridge, J. Alden, A. Zande, J. Parpia, H. Craighead and P. McEuen, *Nano Lett.*, 2008, **8**, 2458–2462.
44 C. Lee, X. Wei, J. W. Kysar and J. Hone, *Science*, 2008, **321**, 385–388.
45 G. T. Mase, R. E. Smelsr and G. E. Mase, *Contunuum Mechanics for Engineers*, CRC Press, 2009.

